Size and shape determination of spheroidal scatterers using two-dimensional angle resolved scattering

Michael Giacomelli, Yizheng Zhu, John Lee, and Adam Wax*

Dept. of Biomedical Engineering and Fitzpatrick Center for Photonics, Duke University, Durham NC 27708, USA
**a.wax@duke.edu*

Abstract: We demonstrate accurate determination of the size and shape of spherical and spheroidal scatterers through inverse analysis of two-dimensional solid-angle and depth resolved backscattered light intensities. Intensity of scattered light is measured over a wide range of solid angles using a novel scanning fiber optic interferometer from both individual and ensembles of scatterers. T-matrix based inverse analysis of these two-dimensional angular measurements yields completely unique size and aspect ratio determinations with subwavelength precision over a large range of possible scatterer geometries.

OCIS codes: (290.0290) Scattering; (290.3200) Inverse Scattering (290.5820); Scattering measurements; (290.5855) Scattering, polarization.

References and links

1. A. Dhar, K. S. Johnson, M. R. Novelli, S. G. Bown, I. J. Bigio, L. B. Lovat, and S. L. Bloom, "Elastic scattering spectroscopy for the diagnosis of colonic lesions: initial results of a novel optical biopsy technique," Gastrointest. Endosc. **63**(2), 257–261 (2006).
2. L. B. Lovat, K. Johnson, G. D. Mackenzie, B. R. Clark, M. R. Novelli, S. Davies, M. O'Donovan, C. Selvasekar, S. M. Thorpe, D. Pickard, R. Fitzgerald, T. Fearn, I. Bigio, and S. G. Bown, "Elastic scattering spectroscopy accurately detects high grade dysplasia and cancer in Barrett's oesophagus," Gut **55**(8), 1078–1083 (2005).
3. V. Backman, V. Gopal, M. Kalashnikov, K. Badizadegan, R. Gurjar, A. Wax, I. Georgakoudi, M. Mueller, C. W. Boone, R. R. Dasari, and M. S. Feld, "Measuring cellular structure at submicrometer scale with light scattering spectroscopy," IEEE J. Sel. Top. Quantum Electron. **7**(6), 887–893 (2001).
4. M. S. Feld, V. Backman, M. B. Wallace, L. T. Perelman, J. T. Arendt, R. Gurjar, M. G. Müller, Q. Zhang, G. Zonios, E. Kline, T. McGillican, S. Shapshay, T. Valdez, K. Badizadegan, J. M. Crawford, M. Fitzmaurice, S. Kabani, H. S. Levin, M. Seiler, R. R. Dasari, I. Itzkan, and J. Van Dam, "Detection of preinvasive cancer cells," Nature **406**(6791), 35–36 (2000).
5. I. Itzkan, L. Qiu, H. Fang, M. M. Zaman, E. Vitkin, I. C. Ghiran, S. Salahuddin, M. Modell, C. Andersson, L. M. Kimerer, P. B. Cipolloni, K.-H. Lim, S. D. Freedman, I. Bigio, B. P. Sachs, E. B. Hanlon, and L. T. Perelman, "Confocal light absorption and scattering spectroscopic microscopy monitors organelles in live cells with no exogenous labels," Proc. Natl. Acad. Sci. U.S.A. **104**(44), 17255–17260 (2007).
6. C. Xu, C. Vinegoni, T. S. Ralston, W. Luo, W. Tan, and S. A. Boppart, "Spectroscopic spectral-domain optical coherence microscopy," Opt. Lett. **31**(8), 1079–1081 (2006).
7. F. Robles, R. N. Graf, and A. Wax, "Dual window method for processing spectroscopic optical coherence tomography signals with simultaneously high spectral and temporal resolution," Opt. Express **17**(8), 6799–6812 (2009).
8. F. E. Robles, and A. Wax, "Measuring morphological features using light-scattering spectroscopy and Fourier-domain low-coherence interferometry," Opt. Lett. **35**(3), 360–362 (2010).
9. J. W. Pyhtila, R. N. Graf, and A. Wax, "Determining nuclear morphology using an improved angle-resolved low coherence interferometry system," Opt. Express **11**(25), 3473–3484 (2003).
10. Y. Zhu, N. G. Terry, and A. Wax, "Scanning fiber angle-resolved low coherence interferometry," Opt. Lett. **34**(20), 3196–3198 (2009).
11. M. G. Giacomelli, K. J. Chalut, J. H. Ostrander, and A. Wax, "Review of the Application of T-Matrix Calculations for Determining the Structure of Cell Nuclei With Angle-Resolved Light Scattering Measurements," IEEE J. Sel. Top. Quantum Electron. **PP**(99), 1–9 (2009).
12. A. M. K. Nilsson, P. Alsholm, A. Karlsson, and S. Andersson-Engels, "T-matrix computations of light scattering by red blood cells," Appl. Opt. **37**(13), 2735–2748 (1998).
13. D. D. Duncan, and M. E. Thomas, "Particle shape as revealed by spectral depolarization," Appl. Opt. **46**(24), 6185–6191 (2007).

#127403 - $15.00 USD Received 3 May 2010; revised 20 Jun 2010; accepted 21 Jun 2010; published 23 Jun 2010

14. J. R. Mourant, T. M. Johnson, S. Carpenter, A. Guerra, T. Aida, and J. P. Freyer, "Polarized angular dependent spectroscopy of epithelial cells and epithelial cell nuclei to determine the size scale of scattering structures," J. Biomed. Opt. **7**(3), 378–387 (2002).
15. J. Ramachandran, T. M. Powers, S. Carpenter, A. Garcia-Lopez, J. P. Freyer, and J. R. Mourant, "Light scattering and microarchitectural differences between tumorigenic and non-tumorigenic cell models of tissue," Opt. Express **15**(7), 4039–4053 (2007).
16. Z. J. Smith, and A. J. Berger, "Validation of an integrated Raman- and angular-scattering microscopy system on heterogeneous bead mixtures and single human immune cells," Appl. Opt. **48**(10), D109–D120 (2009).
17. Y. Zhu, M. G. Giacomelli, and A. Wax, "Fiber-optic interferometric two-dimensional scattering-measurement system," Opt. Lett. **35**(10), 1641–1643 (2010).
18. M. I. Mishchenko, L. D. Travis, and J. W. Hovenier, *Light scattering by nonspherical particles: theory, measurements and applications* (Academic, San Diego; London, 2000).
19. K. J. Chalut, M. G. Giacomelli, and A. Wax, "Application of Mie theory to assess structure of spheroidal scattering in backscattering geometries," J. Opt. Soc. Am. A **25**(8), 1866–1874 (2008).
20. K. J. Chalut, K. Kulangara, M. G. Giacomelli, A. Wax, and K. W. Leong, "Deformation of stem cell nuclei by nanotopographical cues," Soft Matter **6**(8), 1675–1681 (2010).
21. M. I. Mishchenko, L. D. Travis, and D. W. Mackowski, "T-matrix computations of light scattering by nonspherical particles: A review," J. Quant. Spectrosc. Radiat. Transf. **55**(5), 535–575 (1996).
22. M. I. Mishchenko, "Calculation of the amplitude matrix for a nonspherical particle in a fixed orientation," Appl. Opt. **39**(6), 1026–1031 (2000).
23. A. Wax, "Low-coherence light-scattering calculations for polydisperse size distributions," J. Opt. Soc. Am. A **22**(2), 256–261 (2005).
24. J. W. Pyhtila, H. Ma, A. J. Simnick, A. Chilkoti, and A. Wax, "Analysis of long range correlations due to coherent light scattering from in-vitro cell arrays using angle-resolved low coherence interferometry," J. Biomed. Opt. **11**(3), 034022 (2006).
25. C. Amoozegar, M. G. Giacomelli, J. D. Keener, K. J. Chalut, and A. Wax, "Experimental verification of T-matrix-based inverse light scattering analysis for assessing structure of spheroids as models of cell nuclei," Appl. Opt. **48**(10), D20–D25 (2009).

1. Introduction

Analysis of elastically scattered light is a promising method of exploring the microscopic details of cellular and tissue structure to assess health, to measure cellular response to mechanical or chemical stimulus, and to study basic cell biology. This method is highly responsive to changes in cellular geometry and optical properties because the far field scattered intensity pattern from objects of dimension comparable to the wavelength of light is extremely sensitive to small changes in size or shape.

One established light scattering technique, elastic-scattering spectroscopy (ESS), spectrally resolves the intensity of light scattered by cellular organelles, whole cells and bulk tissues to detect changes correlated with disease states [1,2]. Light scattering spectroscopy (LSS) is an alternative light scattering technique that emphasizes analysis of singly scattered photons by rejecting diffusely scattered light. In LSS, singly scattered light is analyzed as a function of wavelength and then used to infer details about scatterer geometry, such as average cell nuclei size and density. Several variations of LSS have been explored including polarization sensitive LSS and scattering angle sensitive light scattering spectroscopy (a/LSS) [3]. Backman and colleagues have used LSS to detect dysplasia of the bladder, cervix, colon and esophagus in vivo by detecting increases in average nucleus size [4]. Other groups have combined LSS with confocal scanning as a means of obtaining depth sectioned spectra in vitro [5].

An alternative method to obtaining depth resolved spectra, spectroscopic optical coherence tomography (SOCT) uses coherence gating to collect only singly scattered photons [6]. Recently, a dual window technique was proposed that combines two short time Fourier transforms to obtain good depth and spectral resolution in a single axial scan [7]. SOCT combined with the dual window method has been shown to accurately detect scatterer morphology [8].

Another depth resolved technique for light scattering measurements is angle-resolved low coherence interferometry (a/LCI) which combines the depth resolution and interferometric detection of OCT with angle resolved and polarization sensitive measurements of singly scattered light. The resulting angle-resolved intensity distributions are then compared to a light scattering model to yield the scattering geometry [9]. The a/LCI technique depends on

#127403 - $15.00 USD Received 3 May 2010; revised 20 Jun 2010; accepted 21 Jun 2010; published 23 Jun 2010

two optical components; a low coherence interferometry scheme to perform depth scans into a turbid sample, and a light scattering model that can be used to fit the scattering measurements and recover the nuclear geometry. Several a/LCI systems have been demonstrated, including time domain reference scanning [9] and Fourier domain acquisition through a scanning fiber [10]. These methods have used both Mie theory, a model for spherical scattering, and the T-matrix, a method for computing aspherical scattering as an inverse model [11].

The T-matrix method has attracted significant attention as an alternative to Mie theory for computing scattered fields. Nielson *et al.* modeled angular scattering from red blood cells [12], Duncan *et al.* showed that variations in depolarization with wavelength were correlated with spheroidal aspect ratio (ratio of polar to equatorial axis) [13], and Mourant *et al.* used spheroids as a model for scattering from both organelles and whole cells [14,15]. In all these techniques, the large range of possible spheroidal scatterers, relative to the number of independent measurements that can be recorded through wavelength or 1D angular scattering, results in a potentially ill-conditioned inverse problem. In contrast, Smith *et al*. developed an integrated Raman and angular-scattering microscope (IRAM) that acquired detailed 2D angle resolved and Raman scattering from single cells, but performed inverse analysis using a spherical model [16]. Expanding on previous work, we have recently introduced a fiber-optic interferometric two-dimensional scattering (FITS) system which resolves the scattered field along both polar and azimuthal axes with precise polarization control and while maintaining depth resolution [17].

In this paper we present an improved form of a/LCI analysis that combines FITS for data acquisition with the T-matrix as a light scattering model to implement a new inverse analysis procedure which effectively uses the additional knowledge obtained by 2D solid angle resolved measurements. In contrast to previous work using 1D a/LCI, FITS provides a significantly better-conditioned inverse problem that is largely free of multiple scatterer fits across a very wide range of spheroidal scatterers. We demonstrate the accuracy and specificity of the new FITS system using phantoms containing spheroidal scatterers that mimic scattering from cell nuclei, first by qualitative comparisons to the T-matrix method, and then by performing inverse analysis. The resulting size and aspect ratio determinations are shown to be essentially free of multiple fits and accurate with subwavelength precision.

2. Experimental setup

The FITS system is based on a novel hybrid Michelson-Sagnac interferometer that coherently mixes Michelson and Sagnac signals for a/LCI [17]. As shown in Fig. 1, the device consists of a highly unbalanced fiber coupler with a splitting ratio of 99.99% to 0.01%, generating three significant signals. Arm 2 receives most of the optical power and illuminates the sample. Angularly scattered light (S_{21}) along (θ, φ) is then collected by Arm 1 by scanning the fiber in the x and y directions over the back focal plane of the lens. The other two signals, R_1 and R_2, are generated by the 4% back reflections at the ends of the fiber. For low coherence interferometry, R_1 and S_{21} are used as the reference and sample signals, respectively. R_2 simply provides a non-interferometric background intensity. At each point, the spectrometer reads out the interferogram produced by R_1 and S_{21}, which is converted to a depth resolved A-scan via a Fourier transform. The choice of R_1 as the reference signal allows complete control over the incident and illumination polarizations, a precondition for two-dimensional measurements. Polarization controllers on the two arms are used to independently set the illumination and collection polarizations.

#127403 - $15.00 USD Received 3 May 2010; revised 20 Jun 2010; accepted 21 Jun 2010; published 23 Jun 2010

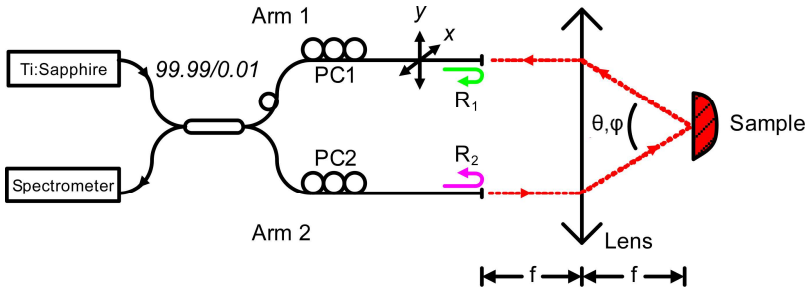

Fig. 1. FITS system used for experimental measurements. 830 nm low coherence light from a Ti:Sapphire laser ($\Delta\lambda$ = 17 nm) is fiber coupled and then divided between two arms of an interferometer via a highly unbalanced fiber coupler with splitting ratio 99.99% to 0.001%. Arm 1 is mechanically scanned across the back focal plane of the lens in two dimensions, resulting in a variable angle pair θ, φ between delivery and collection rays. Polarization controllers PC1 and PC2 provide control over the collection and illumination polarizations respectively. Reflection signal R_1 is path length matched to the sample, while the large path length mismatch between R_2 and the sample generates a high frequency interferometric signal that is not measured due to the finite resolution of the spectrometer.

Scans were performed with 120 points along the y axis, corresponding to a polar angular resolution of 0.22 degrees per depth scan and a maximum polar angle of approximately 25 degrees. Because of the separation of the delivery and collection fibers, the angles within approximately 5.5 degrees of the backscatter angle could not be collected. 180 points were collected along the x axis, corresponding to an azimuthal resolution and range that vary with polar angle, but that at smaller polar angles approach 180 degrees. Depth scans were performed with an axial resolution of 17.7 μm. The total scan time was approximately 12 minutes, due to slow stepper motors and the acquisition rate of our USB spectrometer.

3. T-matrix simulation

3.1 T-matrix

The T-matrix method, also known as the extended-boundary-condition method, is an effective tool for computing exact solutions to scattering problems for spheroidal scatterers [18]. Since few cell nuclei are precisely spherical, the use of a spheroidal model much more accurately estimates the true structure of a scatterer by avoiding inadvertently measuring only one axis [19]. We have shown that using T-matrix as a basis of inverse analysis can capture details about elongation, compression or deformation of cell nuclei that do not change volume [20].

The T-matrix codes provided by Mishchenko et al. were used to generate a database of scattered optical fields for a range of spheroidal scatterers [21]. Individual scatterers were illuminated perpendicular to the spheroidal axis of symmetry with 830 nm monochromatic light. The scattered field was computed from 0 to 359 degrees over the azimuth angle φ, and from 0 to 30 degrees in 0.33 increments over the polar angle θ for a total of 32,400 angular points. At each angle the 4 complex field quantities designated S_{11}, S_{12}, S_{21} and S_{22} corresponding to the in-plane and cross-polarized scattered fields for each illumination polarization [Eq. (1)] were stored in a relational database. In the notation of Mishchenko these field quantities are the solutions to Eqs. (24-28) in [22] for $\alpha = 0$, $\beta = 90$, $\theta = [0,30]$, and $\varphi = [0,359]$ for each scatterer. As an example, S_{11} for a 10 μm spherical scatterer is presented in Fig. 2(a). To build the database, 10,250 different scatterers were simulated, with diameters ranging from 8 μm to 18 μm in 80 nm increments, and aspect ratios between 0.7 (prolate spheroidal) and 1.1 (oblate spheroidal) in steps of 0.005. Refractive index was fixed at 1.58 for polystyrene scatterers, while 1.41 was used for the PDMS media.

3.2 Lens transformation and coordinate systems

The spherical coordinate system centered on the simulated scatterer was propagated to the back focal plane of the imaging optics using a simple matrix operation that maps the

#127403 - $15.00 USD Received 3 May 2010; revised 20 Jun 2010; accepted 21 Jun 2010; published 23 Jun 2010

amplitude of the scattering matrix elements into vector electric field quantities in the image plane:

$$\begin{pmatrix} E_{ss} & E_{sp} \\ E_{ps} & E_{pp} \end{pmatrix} = \frac{e^{ikR}}{kR} \begin{pmatrix} -\cos\varphi & -\sin\varphi \\ -\sin\varphi & \cos\varphi \end{pmatrix} \begin{pmatrix} S_{11} & S_{12} \\ S_{21} & S_{22} \end{pmatrix} \begin{pmatrix} E_p^I \\ E_s^I \end{pmatrix} \quad (1)$$

where E^I represents the incident field components and E with no superscript represents the scattered electric field in the image plane with the first subscript referring to the illumination polarization while the second to the collected polarization. The resulting polarized field values were then resampled evenly in polar space [Fig. 2(b)]. We hereafter use these two-letter combinations to refer to each of these field components. PP and SS are co-polarization scattering signals along the y and x axis respectively while PS and SP are the cross-polarization signals.

3.3 Size distributions and database parameters

The scattered fields produced from the T-matrix simulations represent the distribution generated by a single spheroid illuminated by monochromatic rather than low coherence light. However, distributions in wavelength can be efficiently computed from an adequately sampled array of scatterer sizes by interpolating intermediate scatterer sizes, applying a weighting distribution and then numerically integrating over radius using the equivalence between illumination wavelength and scatter size [23]. We have previously documented this algorithm in detail for ensembles of scatterers [11]. Using this method, a 2.5% wavelength distribution corresponding to the bandwidth of the low coherence source was interpolated over the range of 8.6 μm to 16.3 μm equal spherical volume diameter (EVD) in 50nm increments [Fig. 2(c)].

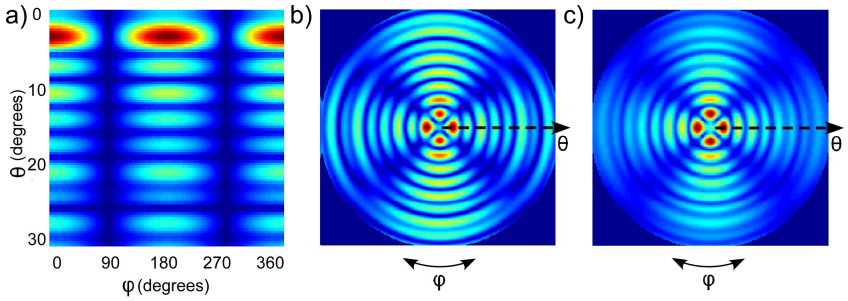

Fig. 2. (a) Absolute value of the S_{11} component of the scattered field for a 10 μm diameter sphere. (b) The E_{pp} component of the scattered field generated by combining the S_{11} and S_{21} fields and converting to polar coordinates. (c) The E_{pp} field after computing a Gaussian weighted wavelength distribution.

Figure 3(a) and 3(b) show the 2D angular scattered fields of spheroids and their dependence on EVD and aspect ratio, respectively.

#127403 - $15.00 USD Received 3 May 2010; revised 20 Jun 2010; accepted 21 Jun 2010; published 23 Jun 2010

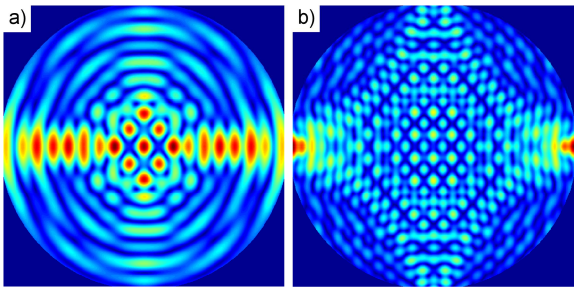

Fig. 3. Still image frames from online video clips showing (a) a 0.9 aspect ratio spheroid expanding from 10 μm to 15 μm EVD (Media 1) and (b) a 15 μm EVD sphere being stretched from spherical to 0.7 aspect ratio (Media 2). Still images are for 10 μm EVD with an aspect ratio of 0.9 and 15 μm EVD with an aspect ratio of 0.8 respectively, both PP polarized.

4. 2D angular scattering results

4.1 Comparison of simulated and experimental results

The FITS system was initially validated by measuring single and ensemble scattering from phantoms containing polystyrene microspheres embedded in polydi-methylsiloxane (PDMS). Figure 4. shows the PP polarized summed intensity projections of depth resolved scans from (a) 15 μm single scatterers, (b) 10 μm ensembles and (c) 6 μm ensembles. It should be emphasized here that these are summed projections over a small range of depths in a 3D volume; individual scans may contain many axially resolved scatterers. Notably, the two distributions for samples with ensemble scatterers contain a high frequency modulation of the Mie scattering pattern, a form of coherent interference that contains information about the distance between scatterers. In contrast to speckle phenomena, the modulation term here presents well defined frequencies which do not overlap with the frequency seen for the individual scatterer patterns, provided the mean scatterer separation is greater than the scatterer diameter [24]. In all three scans, excellent qualitative agreement is obtained between the scans.

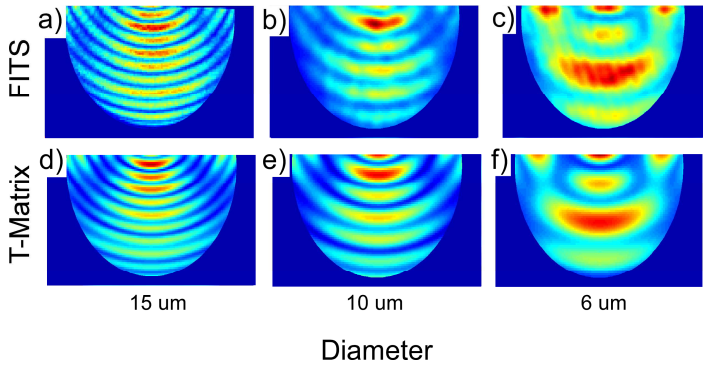

Fig. 4. FITS measured scattering from spherical microspheres with equal volume diameter of (a) 15 μm, (b) 10 μm and (c) 6 μm in PP polarization. (d)–(f) Matching T-matrix simulations. In contrast to the 15 μm sphere example, the distribution from the 10 and 6 μm samples illuminated multiple scatterers concurrently, and so were low pass filtered to reduce high frequency interference fringes due to coherent scattering between particles. Note that this frequency is modulation is deterministic in comparison to speckle observed for random scattering phenomena.

#127403 - $15.00 USD Received 3 May 2010; revised 20 Jun 2010; accepted 21 Jun 2010; published 23 Jun 2010

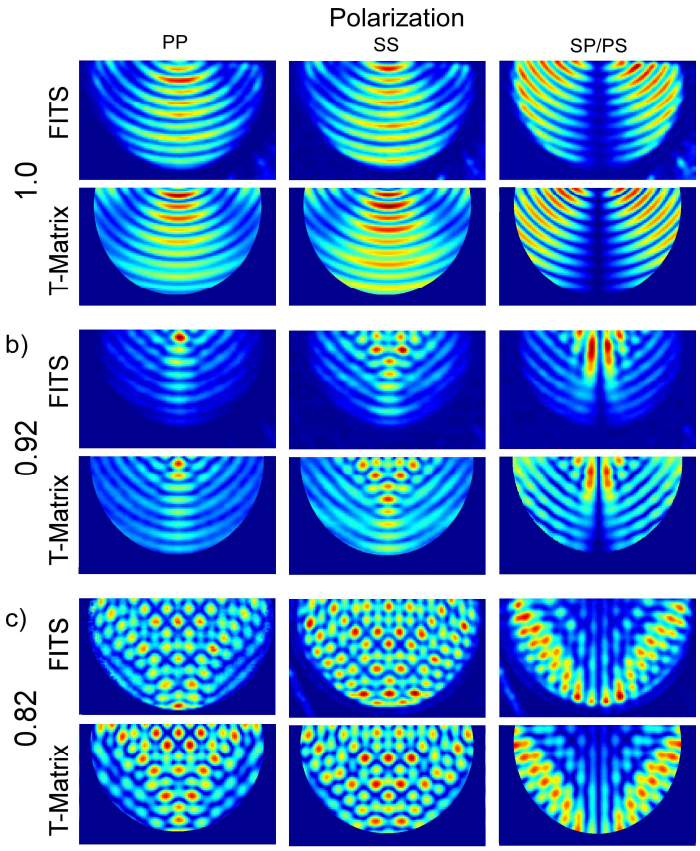

Fig. 5. Qualitative comparison of FITS (odd rows) and T-matrix simulation (even rows) for a 15 μm EVD (a) sphere, (b) prolate spheroid with aspect ratio 0.92, and (c) prolate spheroid with aspect ratio 0.82 as determined by quantitative image analysis (QIA). The two cross polarized cases are identical and thus presented as a single combined plot. The T-matrix simulations have been masked off at the GRIN lens boundaries to limit their angular extent to match the experimental range.

Next, PDMS microsphere phantoms were stretched using a procedure validated previously [25]. Briefly, each phantom was heated past the glass transition point of polystyrene, stretched along one axis, and then allowed to cool into micro-spheroidal shape. The process leaves the EVD unchanged, but decreases the aspect ratio depending on the tension applied. These spheroidal phantoms were used to assess the ability of the FITS system to assess structure of aspherical scatterers. Figure 5 presents co-polarization components SS, PP, and cross-polarization components (PS and SP, only one of which is shown since both are identical in theory and experiments) of the FITS scans from the 15 μm EVD phantom compared with T-matrix simulations calculated based on the sizes determined by QIA for a) a spherical Mie scatterer, b) a slightly spheroidal scatter of aspect ratio 0.92, and c) a moderately spheroidal scatterer of aspect ratio 0.82. Several trends are apparent in these comparisons. First, the PP and SS polarized results generally look similar for all aspect ratios, although the location of the peaks and valleys is typically shifted by about one half cycle between the two. In contrast, the cross polarized SP/PS case is strikingly different, particularly for higher aspect ratios where very little light is directly backscattered. These effects are observable with FITS only because of its high polarization extinction ratio (>20dB). Second, for all polarizations, the patterns appear with a high degree of azimuthal symmetry in the spherical case. In the case of a spherical scatterer, the 2D scan is essentially azimuthally degenerate, as predicted by Mie theory and FITS offers no significant advantage over conventional a/LCI scanning. However, as the scatterers are deformed, symmetry is quickly lost and the inadequacy of Mie theory

#127403 - $15.00 USD Received 3 May 2010; revised 20 Jun 2010; accepted 21 Jun 2010; published 23 Jun 2010

quickly becomes apparent. For the moderately deformed 0.82 aspect ratio phantom, the radial scans separated by even a few degrees of azimuth angle are nearly uncorrelated. Finally, as expected via symmetry, the SP and PS fields were experimentally determined to be identical.

5. Inverse analysis of spheroids

5.1 Image processing, registration and determination of angular range

Each FITS scan consists of 21,600 depth scans each recorded at a unique scattering angle. Because the backscattering angle is not collected, accurate registration of experimental and simulated data is a difficult problem that must account for both slight variation in starting angle and field distortion in the GRIN lens. We have developed a two step algorithm that gives a reasonable co-registration by using a reference phantom with spherical scatterers to map the curvature. In the first step, scattering maxima from the experimental data along the φ = 0 degrees line are combined with a guess of where any specific minima is located along the φ = 45 degrees line [Fig. 6(a)]. In the second step, the initial registration is corrected by refitting along the φ = 0 axis, as well as a perpendicular line of maxima arbitrarily selected along the center of the registered image [Fig. 6(b)]. The final registration is then computed as a projective transform of the two perpendicular lines of maxima from the experimental data to the Mie theory simulations. The resulting co-registered images are adequate for inverse analysis, but still contain noticeable field curvature near the GRIN lens boundaries (Fig. 5), an issue which will be improved in future work.

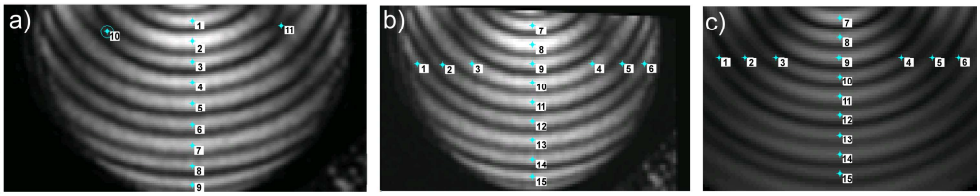

Fig. 6. (a) Experimental data with φ = 0 radial maxima selected, and a single pair of points along the φ = +/–45 line estimated. (b) Experimental data after first stage of registration with common points in simulated data.(c) Simulated data with corresponding points marked. The first round of fitting corrects for a small tilt about the θ = 0 angle, allowing a perpendicular line of points to be selected in the second round.

5.2 Chi squared fitting

The inverse analysis procedure compares the simulated T-matrix data with registered experimental data by computing the χ^2 error:

$$\frac{\sum\left[\mathrm{E}_{\mathrm{measured}}(\theta,\varphi)-\mathrm{E}_{\mathrm{tmatrix}}(\theta,\varphi)\right]^2}{\sum\left[\mathrm{E}_{\mathrm{tmatrix}}(\theta,\varphi)\right]^2} \tag{2}$$

between the measured field and each simulated field in the database. The process involves three distinct steps which have been adapted from analysis of 1D a/LCI data [9]:

(1) The registered experimental data is transformed onto the simulated angular space using a projective transform and the edges of the GRIN lens are masked off to avoid spurious signals.

(2) The experimental data is low pass filtered to remove high frequency oscillations that result from coherent interference of adjacent beads using a procedure developed previously [24]. While these oscillations carry information about the spatial distribution of scatterers within the illumination beam, they are removed to isolate the component of scattering due to individual scatterers.

#127403 - $15.00 USD Received 3 May 2010; revised 20 Jun 2010; accepted 21 Jun 2010; published 23 Jun 2010

(3) An angle-by-angle χ^2 error value [Eq. (2)] is computed between the experimental data and each simulated field. The lowest error value is determined and the corresponding 'best fit' yields the scatterer structure.

Inverse analysis was performed on several phantoms containing scatterers of various geometries. Because the cross-polarization case returned less energy into the backscattering angles, we focused on the in-plane polarizations for simplicity of the analysis. Three representative samples are presented here, a 15 μm sphere (Fig. 7), a 15 μm EVD slightly stretched spheroid (Fig. 8), and a 15 μm EVD moderately stretched spheroid (Fig. 9). All beads had a manufacturer specified diameter of 15.02 μm +/– 80 nm prior to stretching. The analysis of three samples shows extremely good agreement in assessment of both EVD and aspect ratio (Table 1).

Table 1. QIA vs. FITS measurements

	Spherical	Slightly Stretched	Moderately Stretched
FITS EVD (μm)	15.00 ± 0.24	14. 95 ± 0.33	15.00 ± 0.24
QIA Aspect Ratio	1.0	0.93	0.82
FITS Aspect Ratio	0.995 ± 0.04	0.925 ± 0.01	0.825 ± 0.005

Examining the χ^2 error plots across the fitted parameters, shows two apparent trends. First, spherical particles have less complex diffraction patterns than aspherical particles, and therefore provide less information as input to the inverse analysis procedure. Consequently, the best fit for the spherical scatterer produces a χ^2 error which covers a much larger area in parameter space than the spheroidal cases. Second, as scatterers elongate, an oscillatory pattern appears diagonally in which the χ^2 error fluctuates above and below the mean. This corresponds to the algorithm approximately tracking a line along manifolds which keep the major scatterer axis constant. Far away from these lines, the far field patterns are essentially uncorrelated and the χ^2 error remains nearly constant. This effect is contrasted in Figs. 9(b) and 9(c), where the 1D cross sections present cuts along and perpendicular from such a diagonal respectively.

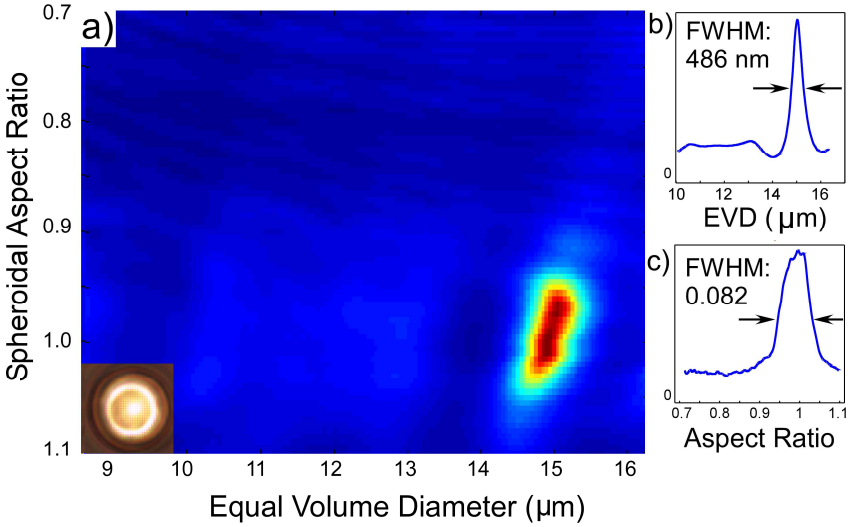

Fig. 7. (a) Relative 2D χ^2 error between light scattered by a 15 μm sphere (phase image bottom left corner) and the database of T-matrix simulated fields. Minimum error is indicated in dark red and occurs at an EVD of 15.00 and an aspect ratio of 0.995. (b) Horizontal slice of 1/ χ^2 error showing the full width half maximum (FWHM) EVD resolution of 0.49 μm, where FWHM is computed relative to the background (uncorrelated) value rather than zero. (c) Vertical slice of 1/ χ^2 error showing the FWHM aspect ratio resolution of 0.082.

#127403 - $15.00 USD Received 3 May 2010; revised 20 Jun 2010; accepted 21 Jun 2010; published 23 Jun 2010

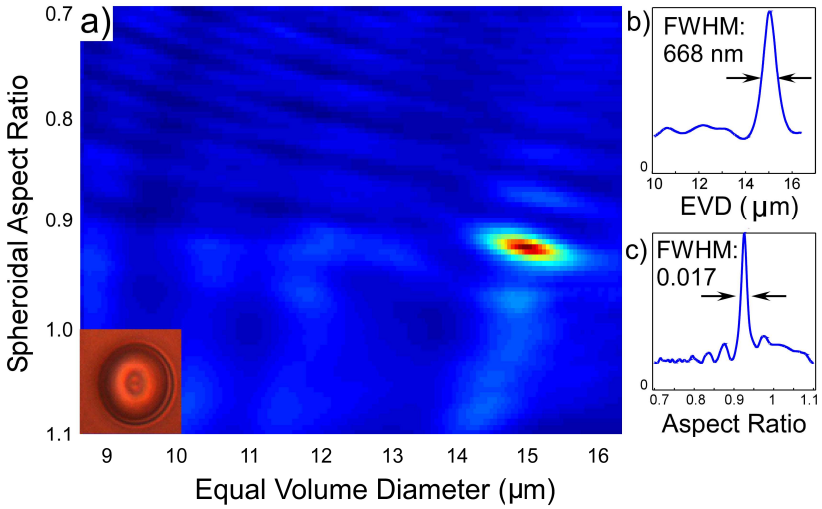

Fig. 8. (a) Relative 2D χ^2 error between light scattered by a 15 μm EVD spheroid with an aspect ratio of 0.92 as determined via QIA (phase image bottom left corner) and the database of T-matrix simulated fields. Minimum error is indicated in dark red and occurs at an EVD of 14.95 and an aspect ratio of 0.925. (b) Horizontal slice of $1/\chi^2$ error showing the full width half maximum (FWHM) EVD resolution of 0.67 μm, where FWHM is computed relative to the background (uncorrelated) value rather than zero. (c) Vertical slice of $1/\chi^2$ error showing the FWHM aspect ratio resolution of 0.017.

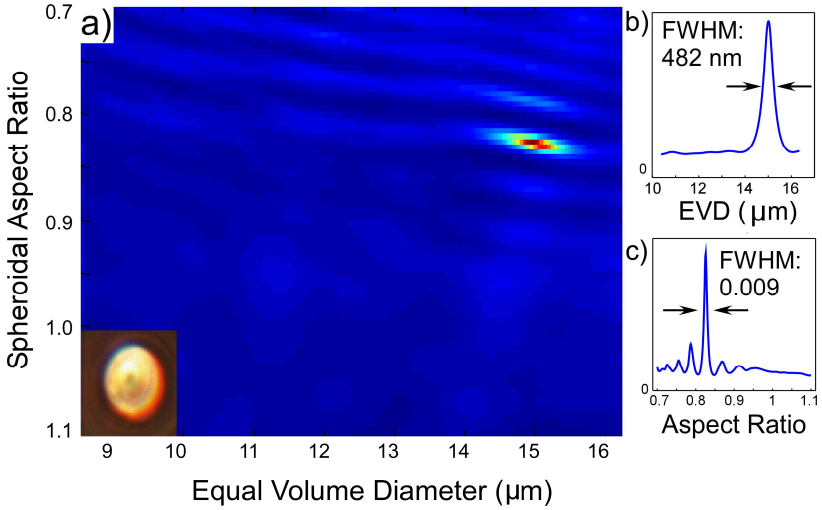

Fig. 9. (a) Relative 2D χ^2 error between light scattered by a 15 μm EVD spheroid with an aspect ratio of 0.82 as determined via QIA (phase image bottom left corner) and the database of T-matrix simulated fields. Minimum error is indicated in dark red and occurs at an EVD of 15.00 and an aspect ratio of 0.825. (b) Horizontal slice of $1/\chi^2$ error showing the full width half maximum (FWHM) EVD resolution of 0.48 μm, where FWHM is computed relative to the background (uncorrelated) value rather than zero. (c) Vertical slice of $1/\chi^2$ error showing the FWHM aspect ratio resolution of 0.009.

6. Discussion

6.1 Solid angle resolved scattering

Traditionally, the applicability of inverse scattering techniques based on wavelength-, angle- or polarization-resolved measurements has been tempered by the limited number of

#127403 - $15.00 USD Received 3 May 2010; revised 20 Jun 2010; accepted 21 Jun 2010; published 23 Jun 2010

independent measurements that can be acquired for a given scatterer, resulting in an inverse problem that may be poorly conditioned and analysis which can produce non-unique solutions. Methods such as a/LCI and LSS have depended on *a priori* knowledge to narrow the range of expected scatterer geometries in order to reduce multiple inverse solutions to one, or at most a few, possible answers. In the absence of such knowledge, these techniques can misinterpret the analysis results by providing numerically optimal, but physically incorrect solutions. Given these limitations, light scattering methods have typically been focused on distinguishing a few possible tissue states over a limited range of geometries which are usually spherical.

In contrast, the huge number of independent measurements, which are possible over even a small range of scattering solid angles, results in a significantly better conditioned inverse problem almost entirely free of non-unique fits across a fairly wide range of geometries. The inverse search range presented here covers a significant fraction of the biologically relevant range of possible spheroidal geometries of cell nucleus scatterers, and is limited primarily by the computer memory in the workstation used for analysis and not by the uniqueness of the fits it provides. Consequently, more powerful forward models than Mie theory are required to fully utilize the available information. In future works, it should be possible to extend the search space of the inverse algorithm to explore additional parameters as well as a much wider range of size and shape parameters. In addition to geometry, the high frequency oscillatory component seen for ensembles of particles can be used to compute relative scatterer spacing and orientation, while the diffraction pattern itself can provide information on the orientation of the particle's long and short axes. It should therefore be possible to explore the polarity and density of clusters of cell nuclei with minimal modification to the procedures presented here. Improved FITS scanning using piezoelectric scanners, a high-speed spectrometer and optimized scan patterns should allow for scan times on the order of a few seconds, opening up the possibility of high throughput and potentially observing dynamic cellular processes.

7. Conclusion

We demonstrated a method for determining scatterer geometry from 2D solid angle-resolved backscattering measurements using the T-matrix method as a light scattering model. As a tool for solid angle resolved scattering, we have employed the FITS system, which exploits the high dynamic range, polarization specificity and depth sectioning of low coherence based techniques such as SOCT and a/LCI. By exploiting these advantages, we have demonstrated size and shape measurements of single and ensembles of microspheroids with subwavelength accuracy and resolution over an extremely wide inverse search space.

Acknowledgments

We gratefully acknowledge the financial support of the US Air Force Research Laboratory under contract #FA8650-09-C-7932 and the National Institute of Health under grant R01CA138594. The views, opinions, and/or findings contained in this article/presentation are those of the author/presenter and should not be interpreted as representing the official views or policies, either expressed or implied, of the Defense Advanced Research Projects Agency or the Department of Defense.

#127403 - $15.00 USD Received 3 May 2010; revised 20 Jun 2010; accepted 21 Jun 2010; published 23 Jun 2010